Ab initio study of vacancy formation in cubic LaMnO3 and SmCoO3 as cathode materials in solid oxide fuel cells

Emilia Olsson, Xavier Aparicio-Anglès, and Nora H. de Leeuw

Citation: The Journal of Chemical Physics **145**, 014703 (2016); doi: 10.1063/1.4954939
View online: http://dx.doi.org/10.1063/1.4954939
View Table of Contents: http://scitation.aip.org/content/aip/journal/jcp/145/1?ver=pdfcov
Published by the AIP Publishing

Ab initio study of vacancy formation in cubic $LaMnO_3$ and $SmCoO_3$ as cathode materials in solid oxide fuel cells

Emilia Olsson,[1] Xavier Aparicio-Anglès,[1] and Nora H. de Leeuw[1,2,a)]
[1]*Department of Chemistry, University College London, London WC1H 0AJ, United Kingdom*
[2]*School of Chemistry, Cardiff University, Main Building, Park Place, Cardiff CF10 3AT, United Kingdom*

(Received 20 April 2016; accepted 11 June 2016; published online 1 July 2016)

Doped $LaMnO_3$ and $SmCoO_3$ are important solid oxide fuel cell cathode materials. The main difference between these two perovskites is that $SmCoO_3$ has proven to be a more efficient cathode material than $LaMnO_3$ at lower temperatures. In order to explain the difference in efficiency, we need to gain insight into the materials' properties at the atomic level. However, while $LaMnO_3$ has been widely studied, *ab initio* studies on $SmCoO_3$ are rare. Hence, in this paper, we perform a comparative DFT + U study of the structural, electronic, and magnetic properties of these two perovskites. To that end, we first determined a suitable Hubbard parameter for the Co *d*–electrons to obtain a proper description of $SmCoO_3$ that fully agrees with the available experimental data. We next evaluated the impact of oxygen and cation vacancies on the geometry, electronic, and magnetic properties. Oxygen vacancies strongly alter the electronic and magnetic structures of $SmCoO_3$, but barely affect $LaMnO_3$. However, due to their high formation energy, their concentrations in the material are very low and need to be induced by doping. Studying the cation vacancy concentration showed that the formation of cation vacancies is less energetically favorable than oxygen vacancies and would thus not markedly influence the performance of the cathode. *Published by AIP Publishing.* [http://dx.doi.org/10.1063/1.4954939]

I. INTRODUCTION

Solid oxide fuel cells (SOFCs) represent an effective and low-emission alternative to traditional power sources.[1–8] Generally speaking, SOFC is composed of three different components: the anode, electrolyte, and cathode. Focusing on the cathode, its main task is to catalyze the oxygen reduction reaction (ORR) and provide an efficient pathway for the oxygen diffusion.[1,4,9–11] It is known that the highest catalytic activity is at the triple phase boundary (TPB) where the gas phase, cathode, and electrolyte meet.[9,12,13] At TPB, O_2 gas is reduced by the cathode, obtaining O^{2-}, which is then driven towards the anode through the electrolyte.

One of the most common class of SOFC cathode materials is perovskite oxides ABO_3, where A is normally lanthanides or alkaline earth metals, and B is usually transition metals from the fourth period.[3,14–22] Lanthanum strontium manganite ($La_{1-x}Sr_xMnO_{3-\delta}$ or LSM) is the typical example of a cathode material. LSM is mainly an electronic conductor, although between 800 °C and 1000 °C, which are the usual SOFC working temperatures, and it also shows ionic conductivity. The ionic conductivity appears also as a result of the strontium doping of the $LaMnO_3$ material. When Sr^{2+} are occupying La^{3+} positions, the charge of the system is compensated by generating oxygen vacancies. These oxygen vacancies are of vital importance for the ionic conduction, because O^{2-} mobility occurs via a vacancy hopping mechanism, as is the case in other materials like yttria-stabilized zirconia or gadolinium-doped ceria.[4,5,23,24]

However, LSM degrades at high temperatures owing to a number of reasons: (i) the thermal stress at the grain boundaries with the electrolyte, leading to crack generation;[25] (ii) the consequent delamination of the electrode from the electrolyte, owing to the thermal stress and oxygen bubbling;[26,27] and (iii) migration of the dopants and impurities to grain boundaries and dislocations, which reduces the effectiveness of the material.[11,13] Therefore, it seems logical that one way to avoid these problems is to reduce the operating temperature, but LSM has been shown to be less efficient under these conditions, with decreased ionic and electronic conductivity.[1,4,11,28,29]

Recently, cobalt-based perovskites have attracted attention owing to their good performance at intermediate temperatures. It is well known that lanthanum cobaltite has higher electronic conductivity than LSM, and more recently samarium cobaltite ($SmCoO_3$) has been reported to show excellent cathode performance at intermediate temperatures.[2,4,9,30–38] Despite being a semiconductor, $SmCoO_3$ possesses temperature-induced insulator-to-metal transitions as well as non-magnetic properties.[31,32,39–43] To enhance its electronic conductivity, $SmCoO_3$ is normally doped on the Co site, leading to mixed valence cobalt centers. The ratio between Co^{3+} and Co^{4+} depends, for example, on the type of dopant, their concentration, or the oxygen partial pressure.[2] Compared to LSM, doping the Co positions with dopants of the same charge does not generate oxygen vacancies but induces a change of the electronic structure, so doped $SmCoO_3$ can become a *p*-type semiconductor, inducing electronic conductivity.

Apart from doping, neutron diffraction analysis has shown that, particularly in the case of $LaMnO_3$, the

a)Author to whom correspondence should be addressed. Electronic mail: deleeuwn@cardiff.ac.uk

material can also contain cation vacancies and these are fully ionized at SOFC operating temperatures.[44,45] Due to the inability of the cubic perovskite materials to accommodate oxygen interstitials in the lattice, cation defects are formed to compensate for the space limitation under high concentrations of oxygen in the lattice.[46–48] Furthermore, it has been shown microscopically that cation migration takes place in LSM cathodes, resulting in grain growth and electrode-electrolyte degradation.[45] In particular, the heat treatment and annealing techniques used during production can lead to the formation of these defects.[48,49] For example, manganese excess is often present in LSM cathodes where it has been shown to decrease electrolyte-electrode degradation.[12] As one of the most popular cathode materials, $LaMnO_3$ is very well-studied from a computational point of view. However, to the best of our knowledge, *ab initio* research on $SmCoO_3$ is rare, since experimental data are not widely available.[31,39,50] Nevertheless, here we present a systematic study in which we have used DFT + U techniques to determine the geometry and electronic structure of $SmCoO_3$. Next, we have studied the effect of introducing oxygen and metal vacancies into this material, as they play an important role in both electronic and ionic conductivities.[51,52] The aim of this work is also to compare these results with $LaMnO_3$, which is therefore also presented in this work for direct comparison.

II. COMPUTATIONAL METHODS

A. Calculation details

The Vienna *ab initio* simulation package, VASP (version 5.3.5),[53–56] was employed for all periodic density functional theory (DFT) calculations. After convergence tests, energy cutoff for $LaMnO_3$ was set at 600 eV, whereas for $SmCoO_3$, it was set at 500 eV. To describe the ion-electron interaction, the projector-augmented wave method (PAW) was applied.[57] Spin-polarized calculations were performed, using the Perdew-Burke-Ernzerhof (PBE)[58,59] functional under electronic and ionic self-consistence, with convergence criteria of 10^{-5} eV and 10^{-3} eV · Å^{-1}, respectively. We have considered the following valence electrons for the atomic species involved: La ($5s^25p^66s^25d^1$), Mn ($3p^63d^64s^1$), Sm ($5s^25p^66s^2$), Co ($4s^23d^7$), and O ($2s^22p^4$). Sm *f*-electrons were included in the pseudopotential. The tetrahedron method with Blöchl corrections for smearing[60] was applied together with a $4 \times 4 \times 4$ Γ-centered Monkhorst-Pack grid.[61] Bader AIM (Atoms in Molecules) charges[62] were calculated using the Henkelman algorithm.[63]

The structural model used throughout this paper is the $2 \times 2 \times 2$ *Pm*-3*m* pseudocubic cell for both $LaMnO_3$ and $SmCoO_3$ (Figure 1) as this was found to be large enough to model bulk properties and defect structures. Perovskites normally crystallize in an orthorhombic structure, but under SOFC and IT-SOFC working conditions, these materials are found in the cubic (*Pm*-3*m*) crystal structure, which is why we chose that one for the present study.

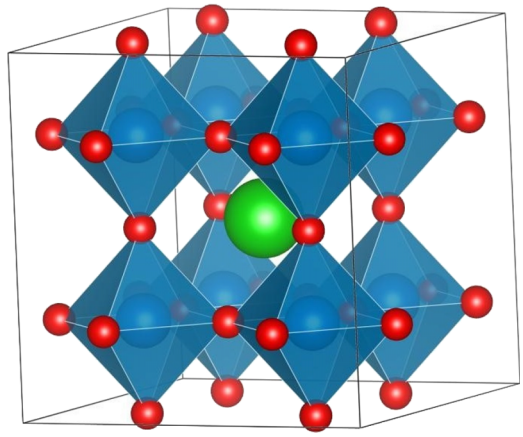

FIG. 1. Polyhedral representation of the cubic perovskite structure. The green atoms are the A-sites, whereas the B-atoms are in the middle of the blue octahedra, and oxygens are red. A atoms are also placed at the center of the edges and faces, but are not shown here for clarity.

B. On-site Coulomb interaction

It is well documented that DFT usually fails when describing the electronic structure of transition metal perovskites. Normal exchange correlation functionals (LDA, or GGA) cannot correct the electron self-interaction problem, leading to a metallic description of perovskites or an underestimation of their band gaps.[64–66] To avoid this problem, we have used the on-site Coulombic interaction (DFT + U) for the 3*d*-electrons in Mn and Co, respectively, which corrects this problem. In this work, we have used Dudarev's approach,[67] in which an effective Hubbard parameter (U_{eff}) is fitted empirically. For $LaMnO_3$, U_{eff} = 4 eV has been applied to Mn *d*-orbitals according to the previous literature.[10] To the best of our knowledge, no U_{eff} parameter has been reported for Co *d*-electrons in $SmCoO_3$. We performed an empirical fitting with respect to its geometric parameters, but results were inconclusive (see Table SI and Figure S1 of the supplementary material). Hence, we decided to use U_{eff} = 3 eV as this value has been previously used for other cobalt-based perovskites.[68,69]

1. Vacancy formation energy

Following the method used for previous studies on perovskites such as $PbTiO_3$,[70] $SrTiO_3$,[71] $La_{1-x}Sr_xFeO_3$,[72] and $BaZrO_3$,[73] the formation of lattice vacancies in the cathode, both cationic and anionic, was evaluated by the defect formation energy at thermodynamic equilibrium. The defect formation energy is commonly calculated using the following formula:[74–76]

$$E_f(j,q) = E_{Defective,q} - E_{Bulk,q} + n_j\mu_j + q(E_v + \Delta E_F), \quad (1)$$

where $E_f(j,q)$ is the defect formation energy for a defect j in a system with charge q. $E_{Defective,q}$ is the total energy of the defective system with charge q, $E_{Bulk,q}$ is the total energy of the non-defective charged system; n_j is the number of removed species j from the bulk, and μ_j is the chemical potential of j.

Charged bulks were computed by changing the total number of electrons in the systems accordingly. In VASP,

one can define the total number of valence electrons. A homogeneous background charge is added to account for the charge, making the system in total neutral and avoiding a diverging Coulomb interaction. Furthermore, finite-size supercell correction schemes for charged defects can be taken into account.[27,30] However, due to the high dielectric constants of the investigated materials (52.71[31] for $LaMnO_3$ and 65.24[32] for $SmCoO_3$), the electrostatic interaction energy between the charged supercells was found to be negligible when using finite-size correction schemes, as these are all inversely proportional to the dielectric constant.[27,28]

As is well documented in the literature, the formation of vacancies may lead to stabilized charge states different from 0, which means that different defect charge states can be accessible.[70,73,76–78] To take this into account, we include the term $q\,(E_v + \Delta E_F)$, where E_v corresponds to the valence band maximum (VBM), which is the Fermi level (E_F), considered to be at 0 eV throughout this work. The term ΔE_F describes the possible positions of the Fermi energy, located between the VBM and the conduction band minimum (CBM), which can be accessible at different energies.

In the particular case of oxygen vacancies, we know that when using DFT the oxygen binding energy is overestimated, and its degree of variation depends on several computational parameters. In order to obtain reliable values that can be compared with the experimental data, the oxygen overpotential correction term should be included in Eq. (1).[10] However, this work intends to perform a comparative study, so that the absolute of this term becomes irrelevant. Finally, thermal, vibrational, and entropic contributions are neglected, as they are known to be smaller than the typical DFT error.[69,79]

2. Chemical potentials

The chemical potential term in Eq. (1) refers to the species that is being removed from the unit cell to generate the vacancy. Given a perovskite with ABO_3 stoichiometry, we know that the chemical potentials must satisfy the following condition:

$$g^{bulk}_{ABO_3} = \mu_A + \mu_B + 3 \cdot \mu_O, \tag{2}$$

where $g^{bulk}_{ABO_3}$ is the free energy per formula unit for bulk ABO_3, and μ_i is the chemical potential of each species. In order to avoid the formation of the respective elementary crystals, we know that each chemical potential must fulfill

$$\Delta\mu_A = \mu_A - g^{bulk}_A \leq 0, \tag{3}$$

$$\Delta\mu_B = \mu_B - g^{bulk}_B \leq 0, \tag{4}$$

$$\Delta\mu_O = \mu_O - \frac{1}{2} g^{tot}_{O_2} \leq 0, \tag{5}$$

where $\Delta\mu_i$ is the chemical potential deviation, g^{bulk}_i is the free energy of element i, and $g^{tot}_{O_2}$ is the free energy of the oxygen molecule ($O_{2(g)}$). It is accepted that $g^{tot}_{O_2}$ can be substituted by the electronic energy of $O_{2(g)}$ (E_{O_2}).[73] This approximation can be made under the assumption that the bulk is in thermodynamic equilibrium with the surface, and the latter is in equilibrium with the gas phase.

The oxygen-rich situation will be determined by Eq. (5) when μ_O is at a maximum, i.e., $\mu_O = \frac{1}{2}E_{O_2}$. On the other hand, the oxygen-poor region will be determined by the formation of the elementary crystals A and B, respectively. In this context, Eq. (2) can be rewritten accordingly

$$\mu_O \geq \frac{1}{3}\left[g^{bulk}_{ABO_3} - g^{bulk}_A - g^{bulk}_B\right] \tag{6}$$

and then, by combination of Eqs. (5) and (6), the limit for the oxygen-poor situation is

$$\frac{1}{3}\Delta G^f_{ABO_3} \leq \Delta\mu_O \leq 0, \tag{7}$$

where $\Delta G^f_{ABO_3} = \left[g^{bulk}_{ABO_3} - g^{bulk}_A - g^{bulk}_B - \frac{3}{2}E_{O_2}\right]$. It is possible to consider the precipitation of intermediate oxides, e.g., AO_2, through their formation free energy,

$$\Delta G^f_{AO_2} > \Delta\mu_A + 2\Delta\mu_O. \tag{8}$$

Once we solve the set of inequalities, a range for chemical potentials will be obtained in which the investigated perovskites are stable. It is worth noting that throughout this work, we considered μ_O and μ_A as independent variables, whereas μ_B is a dependent variable. For $LaMnO_3$, we have considered the formation of the following intermediate oxides: La_2O_3, MnO, MnO_2, Mn_3O_4, and Mn_2O_3, whereas for $SmCoO_3$, we have considered Sm_2O_3, CoO_2, CoO, and Co_3O_4. The detailed list of oxide formation energies is provided in Table SII of the supplementary material. After solving the set of inequalities for each system, we obtained the range of chemical potentials, as depicted in Figure 2.

When we examine the calculated chemical potential phase diagrams, it can be seen that $SmCoO_3$ is unstable under oxygen-rich conditions, which favor the formation of CoO_2. This has also been noted experimentally, with cobalt SOFC cathodes known to be unstable at high oxygen pressures, which validates our model.[80] Therefore, according to Figure 2, the limits for each atomic species are as follows: $-14.10\ \text{eV} \leq \Delta\mu_{La} \leq 0\ \text{eV}$, $-10.02\ \text{eV} \leq \Delta\mu_{Sm} \leq 0\ \text{eV}$, $-4.97\ \text{eV} \leq \Delta\mu_O^{LaMnO_3} \leq 0\ \text{eV}$, and $-4.36\ \text{eV} \leq \Delta\mu_O^{SmCoO_3} \leq -0.5\ \text{eV}$.

Finally, oxygen chemical potentials can be related to the temperature and the partial oxygen pressure according to Eqs. (9)-(11).[71] This approximation relates the term $\Delta\mu_O(T,p)$ to an empirical expression that only considers experimental thermodynamic data,[69]

$$\Delta\mu_O(T,p) = \frac{1}{2}\left\{\Delta G_{O_2}(T,p^0) + k_B T \ln\left(\frac{p}{p^0}\right)\right\} + \delta\mu^0_O \tag{9}$$

with

$$\Delta G_{O_2}(T,p^0) = G_{O_2}(T,p^0) - G_{O_2}(T^0,p^0) \tag{10}$$

and

$$\delta\mu^0_O = \frac{1}{n}\sum\left\{\frac{1}{y}\left(E_{M_xO_y} - xE_M - \Delta H^{f,0}_{M_xO_y}\right) - \frac{1}{2}\left(E^{tot}_{O_2} + T^0 S^{gas}_{O_2}(T^0,p^0)\right)\right\}. \tag{11}$$

In these equations, $G_{O_2}(T,p^0)$ is the tabulated Gibbs free energy for O_2 at a given temperature (T) and standard pressure

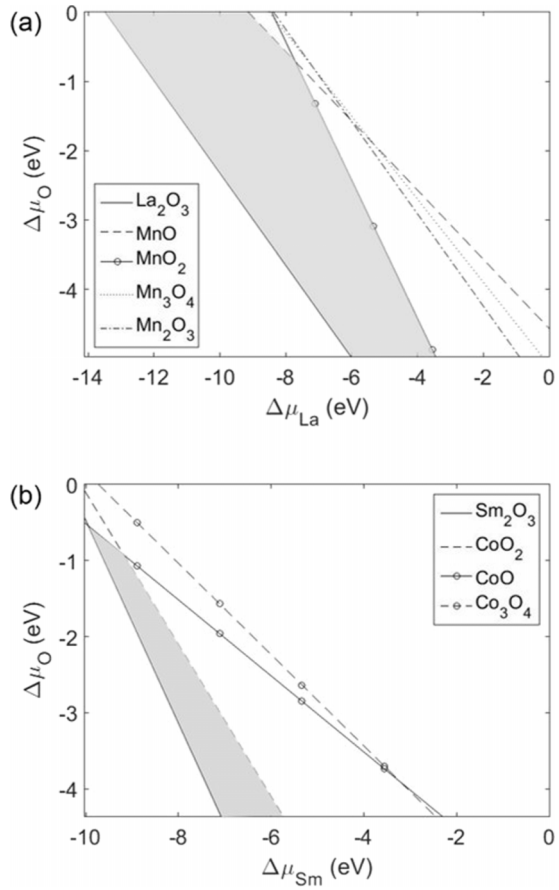

FIG. 2. Chemical potential phase diagram for (a) $LaMnO_3$ and (b) $SmCoO_3$. The grey areas represent the range of chemical potentials in which the perovskites are stable.

(p^0); k_B is the Boltzmann constant (8.6173×10^{-5} eV · K^{-1}), p is the pressure, T^0 is the standard temperature, and $S^{gas}_{O_2}(T^0, p^0)$ is the tabulated entropy of O_2 gas.[81] The term $\delta\mu^0_O$ is a correction term that compensates the deviation between the experimental and the computational data.

III. RESULTS AND DISCUSSION

A. Analysis of the geometry and electronic structure of $LaMnO_3$ and $SmCoO_3$

In order to validate our Hubbard parameters, we have analyzed and compared the geometry and the electronic structure of $LaMnO_3$ and $SmCoO_3$ with available experimental data. Calculated lattice parameters and distances show very good agreement with experimental results, as shown in Table I, with variation of only 0.04-0.03 Å for La–O and Mn–O, respectively, and a surprisingly perfect match between experimental and computed distances for $SmCoO_3$.

The projected density of states (PDOSs) of $LaMnO_3$ shows a half-metallic ferromagnetic structure with a β band gap of 1.58 eV calculated from the Fermi level, and a β^{CBM}-β^{VBM} band gap of 3.38 eV (Figure 3(a)). This behavior has been reported in previous studies.[10] The calculated magnetic moment of the Mn centers is 3.93 μ_B, indicating a high spin state (HS, $t^3_{2g}e^1_g$, $S = 2$) in agreement with the PDOS, in which α-t_{2g} is fully occupied, α-e_g orbitals are half occupied, and β-t_{2g} and β − e_g are unoccupied. Furthermore, the O 2p-orbitals in $LaMnO_3$ are degenerate with the Mn 3d-states, which agrees well with the previously published literature.[22,64]

The $SmCoO_3$ PDOS (Figure 3(b)) shows non-magnetic semiconductor behavior, as α and β states are symmetric and the band gap is 0.68 eV. This agrees with reported experimental information about the $SmCoO_3$ magnetic behavior, although no precise data regarding its bandgap were available.[32,40] However, it has been reported that the band gap of the related perovskite $LaCoO_3$ is 0.6 eV,[84] which suggests that our results are consistent with those of other lanthanide cobalt oxide perovskites. The magnetic moment of Co atoms is 0 μ_B, i.e., Co is in its low spin state (LS,$t^6_{2g}e^0_g$,$S = 0$), which is also observed in the PDOS for $SmCoO_3$, where t_{2g} states are fully occupied whereas e_g states are unoccupied. In conclusion, the Hubbard parameters are used for the two materials to describe their electronic, magnetic, and structural features with acceptable accuracy.

B. Lattice vacancies

Ionic conduction depends, among other factors, on the number of the oxygen vacancies, which in turn depends on the oxygen chemical potential. A low oxygen chemical potential enhances the creation of oxygen vacancies, whereas high oxygen chemical potentials may lead to the creation of cation vacancies. Cation vacancies originate as a result of the fabrication process or as a consequence of the different chemical potentials. Figure 4 shows a schematic of the three types of vacancies investigated in this work.

TABLE I. Calculated and experimental lattice parameter (a); metal–oxygen distances, where A refers to La and Sm, and B to Mn and Co, respectively; and band gap (E_g). Distances are represented in Å and energies in eV.

System		a (Å)	A–O (Å)	B–O (Å)	E_g (eV)
$LaMnO_3$	Experimental[51,18]	3.90[45]	2.74[45]	1.94[45]	1.7[15]
	DFT + U	3.94	2.78	1.97	0 (α) 1.58 (β) 3.38 (β^{CBM}-β^{VBM})
$SmCoO_3$	Experimental	3.75[31,82,83]	2.65[31,82,83]	1.88[31,82,83]	...
	DFT + U	3.75	2.65	1.88	0.68

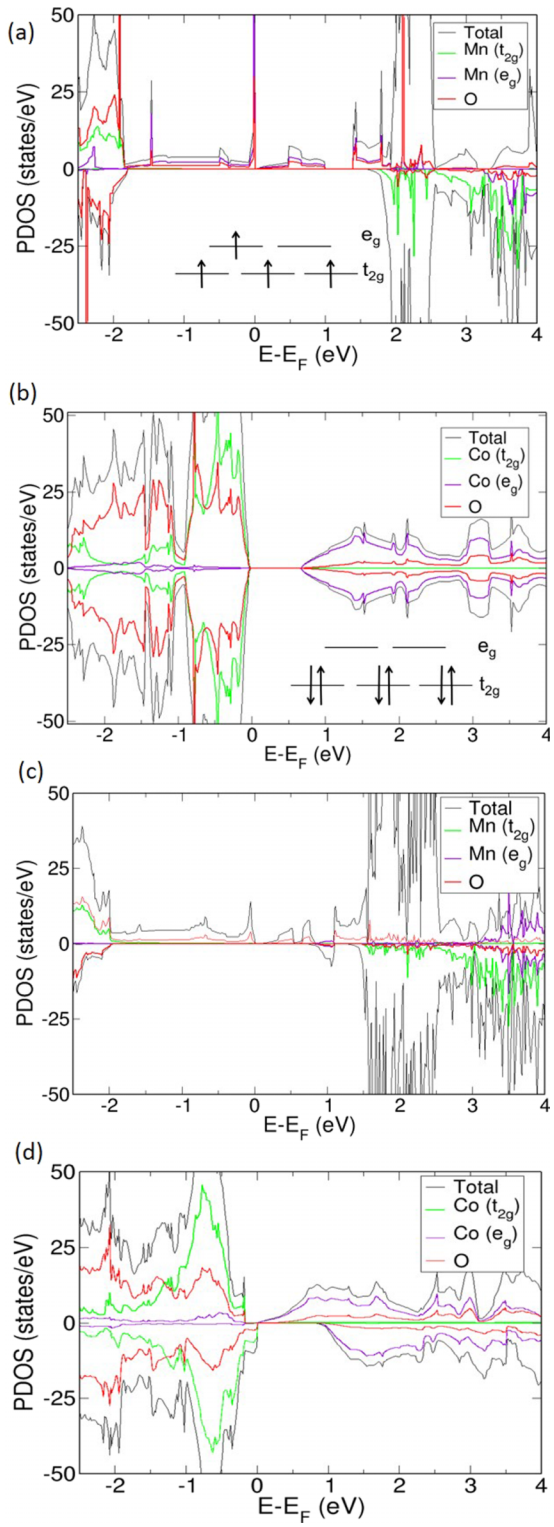

FIG. 3. Projected densities of states (PDOS) for (a) $LaMnO_3$, and (b) $SmCoO_3$, with a schematic representation of the d-orbital occupations in (a) the high spin state of Mn d-electrons, and (b) the low spin state of Co d-electrons. (c) and (d) are the PDOS after the introduction of an oxygen vacancy in $LaMnO_3$ and $SmCoO_3$, respectively. (a) and (b) are in the neutral charge state.

1. Oxygen vacancies

The presence of oxygen vacancies leads to non-significant distortions of both $LaMnO_{(3-x)}$ and $SmCoO_{(3-x)}$ lattices,

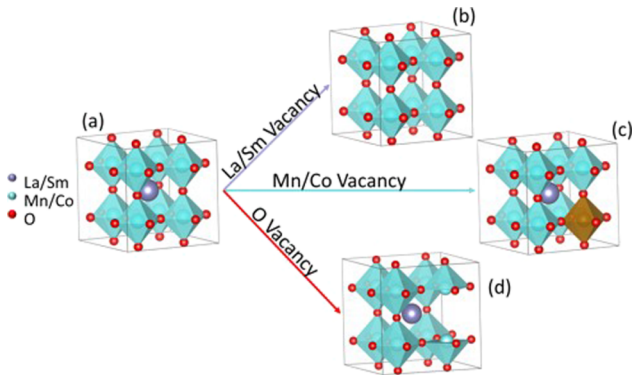

FIG. 4. Polyhedral representation of the crystal structures of both $LaMnO_3$ and $SmCoO_3$ in (a) bulk, (b) A-site cation vacancy, (c) B-site cation vacancy, and (d) oxygen vacancy. Grey spheres represent La and Sm, red spheres oxygen, and blue polyhedra have Mn and Co centered in them.

mainly localized in the atoms neighboring the vacancy, as shown in Table II. In $LaMnO_3$, Mn–O bonds shorten by about 0.06 Å, whereas in $SmCoO_3$, Co–O bond changes are barely noticeable, with a lengthening of only 0.02 Å. We observe the same trends in the A–O distances. La–O bonds are lengthened by 0.13 Å whereas Sm–O only lengthens by 0.02 Å. It is commonly accepted that, for the same type of material, larger distortions indicate a more covalent bonding character, whereas minor distortions show a greater ionic contribution. Thus, according to our results, $SmCoO_3$ has more ionic character than $LaMnO_3$.

As to the electronic and magnetic structures, changes are noted in both materials with the introduction of an oxygen vacancy, as shown in Figures 3(c) and 3(d), respectively. In $LaMnO_3$, the presence of an oxygen vacancy does not significantly alter its electronic structure. The only noticeable difference is that the β band-gap is slightly reduced, as some states are now found at 2.6 eV. Moreover, Mn magnetic moments do not significantly differ from the non-defective bulk, although the Mn that is next nearest neighbors (NNN) of the oxygen vacancy shows a slightly higher magnetic moment, as shown in Table III, coinciding with a small decrease of charge shown by NNN Mn centers compared to those adjacent of the oxygen vacancy.

On the other hand, the presence of an oxygen vacancy in $SmCoO_3$ alters not only the electronic structure of the system but also the Co magnetic moment. The system now shows half-metallic behavior in which the valence band is described

TABLE II. Calculated metal-oxygen distances next to vacancies for non-defective and defective $LaMnO_3$ and $SmCoO_3$.

Material	Vacancy	A–O distance (Å)	B–O distance (Å)
$LaMnO_3$	None	2.78	1.97
	O	2.91	1.91
	La	2.72	1.91
	Mn	2.72	1.86
$SmCoO_3$	None	2.65	1.88
	O	2.67	1.89
	Sm	2.66	1.86
	Co	2.66	1.79

TABLE III. Magnetic moments of the transition metal ion (μ_B) in μ_B and Bader charges (q) in e in the 2×2×2 cubic supercell before and after the creation of lattice vacancies. * indicates ion adjacent to vacancy site. All other values are averaged over the number of species.

	$LaMnO_3$				$SmCoO_3$			
	Bulk	V_O	V_{La}	V_{Mn}	Bulk	V_O	V_{Sm}	V_{Co}
μ_B	3.93	4.05	3.61	3.52	0.0	0.24	0.02	0.84
μ_B^*		3.93	3.61	3.43		0.58	0.02	0.12
q_B	+1.81	+1.60	+1.78	+1.89	+1.31	+1.26	+1.32	+1.40
q_B^*		+1.54	+1.78	+1.80		+1.10	+1.32	+1.36
q_A	+2.12	+2.10	+2.14	+2.09	+2.01	+2.07	+2.12	+2.09
q_O	−1.31	−1.29	−1.24	−1.26	−1.11	−1.16	−1.05	−1.11

by the Co-t_{2g} orbitals and the conduction band by the Co-e_g orbitals. Second, the magnetic moments of Co centers that are nearest neighbors (NN) to the oxygen vacancy increase from 0 to 0.58, whereas the rest of the Co atoms are around 0.24, which agrees well with the calculated Bader charges, which are lower for NN Co compared to NNN Co atoms.

Magnetic moments and Bader charges suggest that, as stated in previous publications,[46] the generation of an oxygen vacancy is related to the reduction of two neighboring Mn/Co atoms, which can be represented as

$$O^{2-} + 2Mn^{3+} \rightarrow \frac{1}{2}O_2 + 2Mn^{2+} \tag{12}$$

or according to the Kröger-Vink notation as[85]

$$O_O + 2Mn_{Mn}^{x} \rightleftharpoons V_O^{\cdot\cdot} + \frac{1}{2}O_2 + 2Mn_{Mn}^{\cdot} \tag{13}$$

which can be understood as the formation of an Mn^{2+}–V_O–Mn^{2+} cluster, and equally applied to Co^{2+}.[46] We verified the existence of these clusters by calculating the spin density ($\Delta\rho^{\alpha-\beta}$) difference, defined as $\Delta\rho^{\alpha-\beta} = \rho^{\alpha-\beta}_{ABO_{3-x}} - \rho^{\alpha-\beta}_{ABO_3} - \rho^{\alpha-\beta}_{O}$, where $\rho^{\alpha-\beta}_{ABO_3}$ is the spin density for the bulk material, $\rho^{\alpha-\beta}_{ABO_{3-x}}$ is the spin density of the defective bulk, and $\rho^{\alpha-\beta}_{O}$ is the spin density of a single oxygen atom, calculated in its triplet state. The representation of $\Delta\rho^{\alpha-\beta}$ is shown in Figure 5 where the increase of spin density is represented by the yellow isosurface, whereas depletion is represented by the blue isosurface. It is worth noting that for both materials, the spin depletion observed in the oxygen vacancy is owing to the fact that we calculated the single oxygen in its triplet state.

In the case of $LaMnO_{3-x}$ (Figure 5(a)), we observe a spin redistribution on the Mn that is NN to the oxygen vacancy, and a very small increase on the rest of the Mn, which fully agrees with the magnetic moments and Bader charges previously discussed. However, the formation of the Mn^{2+}–V_O–Mn^{2+} clusters is not quite evident. In $SmCoO_{3-x}$ (Figure 5(b)), we do see an increase in spin density in all Co centers, but with a larger isosurface in those that are NN to the oxygen vacancy, clearly showing the formation of the reduced Co–V_O clusters.

Oxygen vacancy formation energies ($E_f^{V_O}$) were calculated for five different defect charge states: 0, ±1, and ±2, under the O-rich regime (Table IV and Figure 7). These charge states have been selected as the formal oxygen anion charge is −2. Likewise, the oxygen-rich regime was selected as experimental studies are performed at high oxygen partial pressure and temperature. For CBM, we have used the calculated band gap for $SmCoO_3$ and the β-direction band gap of 1.58 eV for $LaMnO_3$.

As expected, all formation energies are positive, clearly indicating that oxygen vacancies will not be formed spontaneously. However, the formation of oxygen vacancies in $SmCoO_3$ is slightly more favored. For example, if we consider the neutral charge state, in $LaMnO_3$ $E_f^{V_O}$ = 3.14 eV, whereas in $SmCoO_3$ it is 2.08 eV, i.e., more than 1 eV smaller.

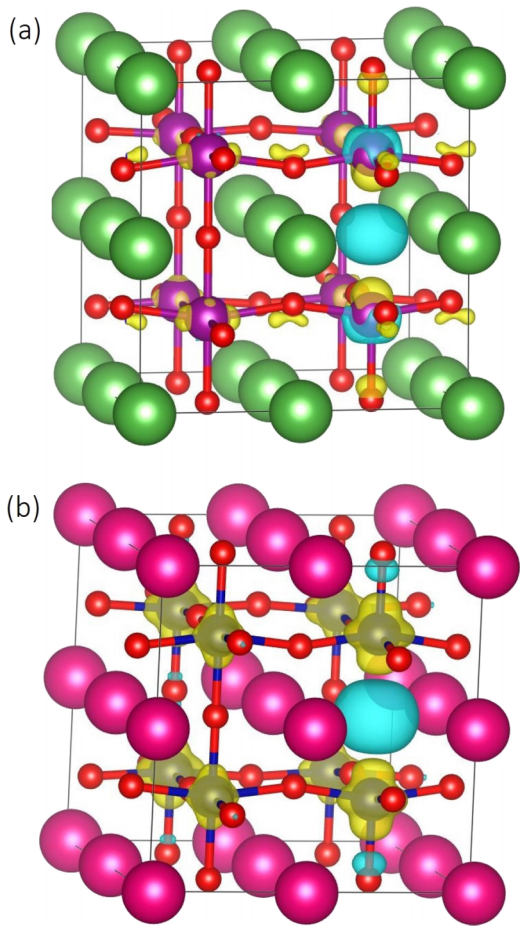

FIG. 5. Spin density difference ($\Delta\rho^{\alpha-\beta}$) representation of (a) $LaMnO_3$ and (b) $SmCoO_3$ with oxygen vacancy in the neutral charge state. Yellow $\Delta\rho^{\alpha-\beta}$ isosurface represents an increase of spin density, whereas blue $\Delta\rho^{\alpha-\beta}$ isosurface represents a spin density depletion. Isosurface value is set at 0.02.

TABLE IV. Oxygen vacancy formation energies (in eV) for $LaMnO_3$ and $SmCoO_3$ for different charge states at the valence band maximum (E_f^{VBM}) and at the conduction band minimum (E_f^{CBM}) under oxygen rich conditions.

	$LaMnO_3$		$SmCoO_3$	
q	E_f^{VBM}	E_f^{CBM}	E_f^{VBM}	E_f^{CBM}
+2	3.15	6.31	0.30	1.65
+1	3.09	4.67	1.46	2.14
0	3.14	3.14	2.08	2.08
−1	3.24	1.66	2.64	1.96
−2	3.91	0.75	2.99	1.64

We have also analyzed the influence of temperature and pressure on the oxygen vacancy formation energy as described in Eq. (1) for the non-charged states for both $LaMnO_{3-x}$ and $SmCoO_{3-x}$ according to Eqs. (9)-(11) (see Figure 6). For

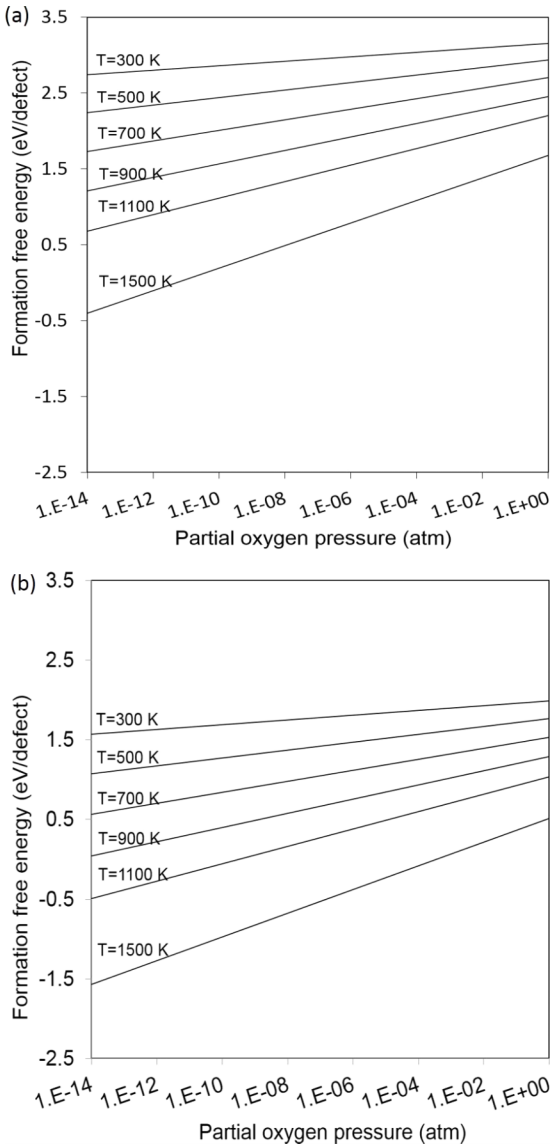

FIG. 6. Oxygen vacancy formation energy as a function of partial oxygen pressure (atm) at different temperatures for (a) $LaMnO_3$ and (b) $SmCoO_3$.

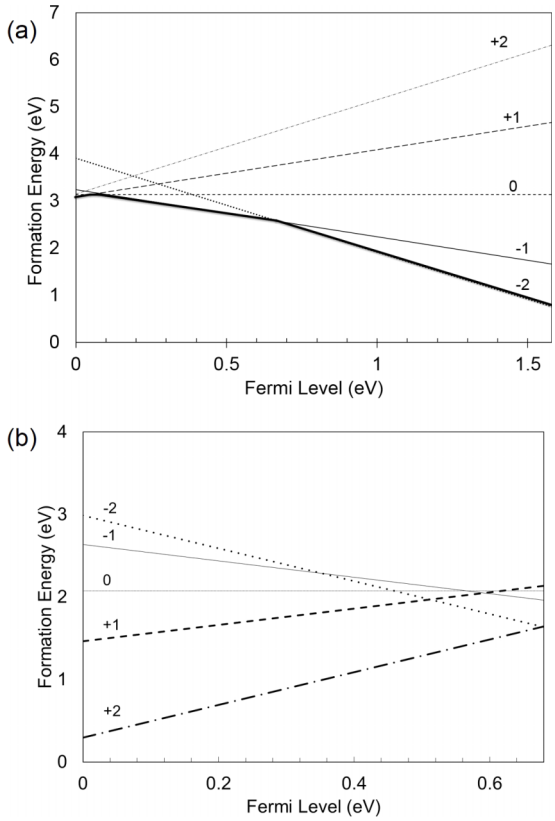

FIG. 7. Oxygen vacancy formation energy in different charge states as a function of the Fermi level for (a) $LaMnO_3$ and (b) $SmCoO_3$. For the $LaMnO_3$, VBM, $\Delta E_F = 0$ eV and CBM, $\Delta E_F = 1.58$ eV, whereas for $SmCoO_3$, VBM, $\Delta E_F = 0$ eV and CBM, $\Delta E_F = 0.68$ eV.

$LaMnO_{3-x}$ Figure 6 shows that the generation of oxygen vacancies is only spontaneous at temperatures higher than 1100 K in combination with low oxygen partial pressure. In $SmCoO_{3-x}$, oxygen vacancies can be spontaneously generated at lower temperatures than $LaMnO_3$, but again at low oxygen partial pressure, which as we have stated already, are not the working conditions in SOFC.

Considering the different charge states, collected in Table IV and Figure 7, we note that the +1 charge state for $LaMnO_3$ has the smallest $E_f^{V_O}$ for $\Delta E_F = 0$ eV. Charge transitions occur when $E_f^{V_O}$ for different charge states intercross at a given energy.[86] The first charge transition is at $\Delta E_F = 0.05$ eV and corresponds to the transition from +1 to 0, almost at the same ΔE_F in which the transition from 0 to −1 occurs, 0.06 eV. The last observed transition happens at $\Delta E_F = 0.67$ eV, from −1 to −2. To get an idea of the thermal cost of these transition energies, we can use the relation $\Delta E_F = k_B T$. Thus, the transition from $+1/0$ occurs at approximately 580 K, $0/-1$ at 696 K, and the transition $-1/-2$ at 7775 K. The last transition is thermally inaccessible at working temperatures and far above the melting point of $LaMnO_3$. We can conclude that at working temperatures, the charge state that is stabilized is $q = -1$, although due to the small energy difference between $+1/0$ and $0/-1$ charge transitions (only 0.01 eV), it is likely that the three charge states, +1, 0, and −1 coexist.

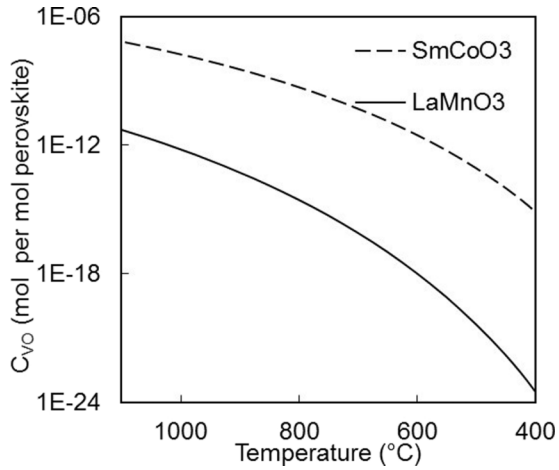

FIG. 8. Oxygen vacancy concentration (mol per mol perovskite) as a function of temperature in $SmCoO_3$ (dashed line) and $LaMnO_3$ (full line), assuming oxygen rich conditions.

In contrast, $SmCoO_{3-x}$ shows a completely different trend, with a preferential charge state of +2 and no accessible charge transitions. This indicates that $SmCoO_{3-x}$ cannot accommodate the two electrons resulting from the oxidation of O^{2-}, i.e., $SmCoO_{3-x}$ cannot act as an effective electron conductor at intermediate temperature SOFC working temperatures, which agrees with the literature.[38,80,87–89]

Finally, using the vacancy formation energy at neutral charge state, we can calculate the concentration of the oxygen vacancies (C_{V_O}) per mole of perovskite according to the following formula:[68,74,90]

$$C_V = N\exp\left(\frac{-E_f^{V_O}}{k_B T}\right), \tag{14}$$

where $E_f^{V_O}$ is the oxygen vacancy formation energy (Table IV), N is the concentration of atomic sites substituted by the defect, which for oxygen vacancies is $N = 3 - C_{V_O}$.[68,74] We calculated the concentration for both $LaMnO_{3-x}$ and $SmCoO_{3-x}$, as shown in Figure 8. We observe that C_{V_O} under equilibrium conditions is higher in $SmCoO_3$ than in $LaMnO_3$, as we would expect from their formation energies. However, vacancy concentrations in $SmCoO_{3-x}$ are still below 1×10^{-6} mol × (mol perovskite)$^{-1}$, and even smaller in $LaMnO_{3-x}$, where they are found below 1×10^{-11} mol × (mol perovskite)$^{-1}$. These results are expected, as we know that experimentally, oxygen vacancies are obtained mainly by doping both materials. Nevertheless, we could also modify the oxygen chemical potential by means of reducing the p_{O_2}.

TABLE V. Cation vacancy formation energies (in eV) for $LaMnO_3$ and $SmCoO_3$ in their neutral charge state.

Material	Vacancy	E_f^V
$LaMnO_3$	La	6.95
	Mn	5.74
$SmCoO_3$	Sm	7.98
	Co	5.17

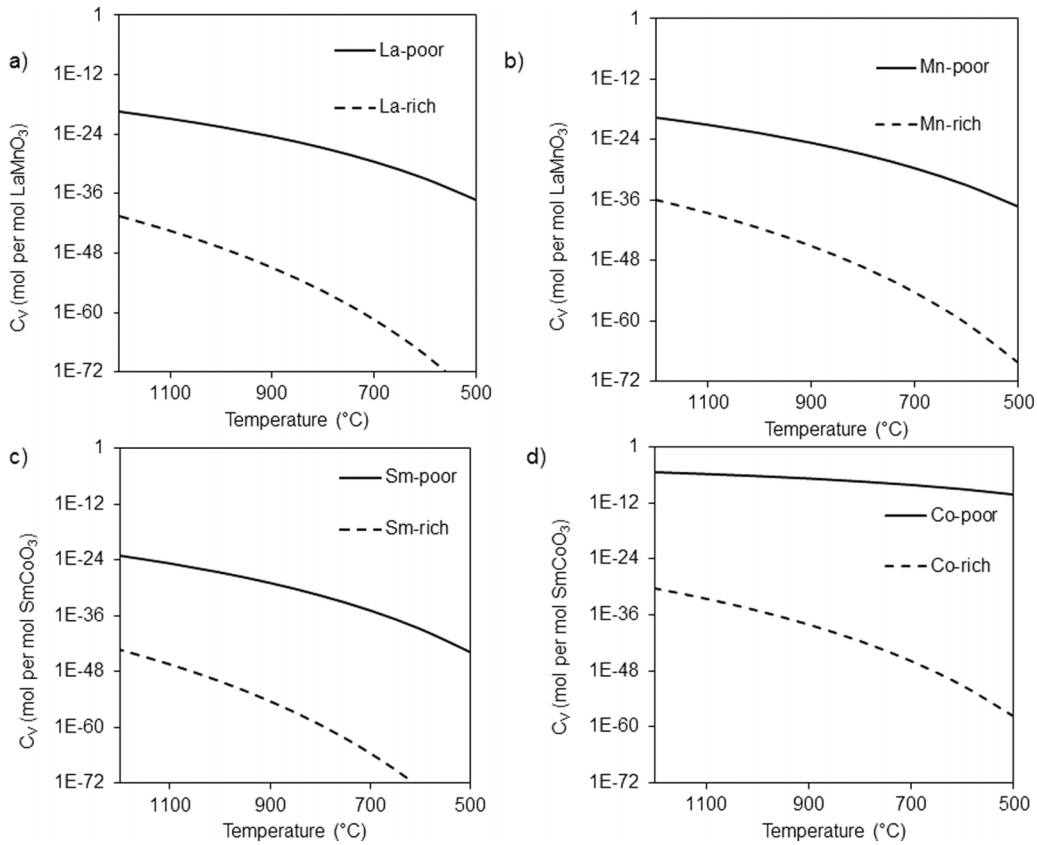

FIG. 9. (a) Lanthanum, (b) manganese, (c) samarium, and (d) cobalt vacancy concentrations versus temperature.

2. Cation vacancies

Finally, we also evaluated the cost of generating cation vacancies in both materials. To that end, and using Eq. (1), we calculated the cation vacancy formation energies for both cations in both materials for the charge states between −3 and +3. E_f^V for neutral charge state are listed in Table V and the rest of the charge states can be found in Table SIII of the supplementary material. We assumed oxygen- and cation-rich conditions for all cases.

As expected, all vacancy formation energies are highly positive, although for the B position (Mn and Co, respectively) they are between 1 and 2 eV smaller than the A position. In any case all energies are higher than 5 eV, which indicates that vacancies will not generate spontaneously. As to the charge states, all cation vacancies are negatively charged, as shown in Table SIII of the supplementary material. For lanthanum, the vacancy formation energy shows only one charge transition, $-2/-3$ at 0.21 eV, which is thermally inaccessible. For the samarium vacancy, the −3 charge state is most stable, with no observed charge transitions, agreeing with the previous literature.[44] Looking at the $B-$ site vacancies, only one charge transition is observed for the manganese vacancy, $-1/-2$ at 0.36 eV. This transition is not thermally accessible during device operation, leaving the charge state of the system as −1. For the cobalt vacancy, the most stable charge state is −3, a charge state that has also been calculated to be the most stable for both cation vacancies in $SmCoO_3$.

Despite this possible influence of cation vacancies on the electronic conductivity, defect concentrations calculated from their vacancy formation energy indicate that in fact, these vacancies are very unlikely. As shown in Figure 9, and using Eq. (14) with $N = 1 - C_V$, cation concentrations under both rich and poor conditions are found below 1×10^{-10} mol · (mol perovskite)$^{-1}$ in almost all cases. The only exception is observed for Co vacancies under Co-poor conditions, which are not however found under experimental conditions. Hence, we can conclude that cation vacancies do not play any key role in the cathode properties, as their concentrations will be extremely low.

IV. CONCLUSION

In this paper, we have used DFT+ U techniques to complement the scarce experimental data available on $SmCoO_3$ and to perform a comparative study with the well-known $LaMnO_3$. For $LaMnO_3$, we were able to successfully reproduce its main properties using already published Hubbard parameters, describing $LaMnO_3$ as a half-metallic perovskite with ferromagnetic behavior. In the case of $SmCoO_3$, with $U_{eff}^{Co(d)} = 3$ eV, we concluded that this perovskite is a semiconductor with a band gap of 0.68 eV and non-magnetic structure, due to the low spin state of all Co centers. Comparatively, $SmCoO_3$ appears to have more ionic character than $LaMnO_3$.

To model lattice vacancies, we calculated the range of chemical potentials in which the materials are stable, obtaining results in agreement with experimental evidence on stability. We found that the oxygen vacancy formation energy for $LaMnO_3$ is higher than for $SmCoO_3$, but that they are all positive, indicating that the formation of V_O is not spontaneous, unless we move into an oxygen-poor regime. The presence of V_O did not significantly affect the electronic structure of $LaMnO_3$, but it did alter the electronic and magnetic properties of $SmCoO_3$. V_O in $SmCoO_3$ turned this semiconductor into a half-metallic material, with the formation of Co^{2+}–V_O–Co^{2+} clusters. In comparison, these clusters were not evident in $LaMnO_3$. The investigation of the charge states indicated that at SOFC working temperatures, $LaMnO_3$ showed stabilization of a negative charge whereas $SmCoO_3$ was not able to accept extra charge, which explained the different experimental behavior observed for both materials regarding electronic conductivity. We also calculated the equilibrium C_{V_O}, showing as expected that it is very low, although $SmCoO_3$ shows higher concentrations, related to its lower vacancy formation energy.

Finally, we studied the formation of cation vacancies, but we found that they require very high energies to be formed. Thus, it is expected that these will only exist in very small concentrations and will have negligible impact on the electronic and ionic conduction in the materials.

Future work will include investigation of anion vacancy behavior in doped materials.

SUPPLEMENTARY MATERIAL

See supplementary material for a graph showing the band gap dependence on U_{eff}-parameter (Figure S1), a comparison of Co PBE functionals and U_{eff} in relation to lattice parameter and band gap (Table SI), calculated and experimental metal oxide formation energies and enthalpies (Table SII), and cation vacancy formation energies (Table SIII).

ACKNOWLEDGMENTS

The authors acknowledge the Engineering and Physical Sciences Research Council (EPSRC) for financial support (Grant Reference No. EP/K016288/1). We also acknowledge the use of the UCL Legion High Performance Computing Facility (Legion@UCL) in the completion of this work. Finally, via our membership of the UK's HPC Materials Chemistry Consortium, which is funded by EPSRC (Grant No. EP/L000202), this work made use of the facilities of ARCHER, the UK's national high-performance computing service, which is funded by the Office of Science and Technology through EPSRC's High End Computing Programme. N.H.d.L. thanks the Royal Society for an Industry Fellowship. E.O. gratefully acknowledges EPSRC funding of Centre for Doctoral Training (Grant No. EP/G036675/1).

[1]R. M. Ormerod, Chem. Soc. Rev. **32**, 17 (2003).
[2]X. Jiang, Q. Xu, Y. Shi, X. Li, W. Zhou, H. Xu, and Q. Zhang, Int. J. Hydrogen Energy **39**, 10817 (2014).
[3]L. Malavasi, C. A. J. Fisher, and M. S. Islam, Chem. Soc. Rev. **39**, 4370 (2010).
[4]S. M. Haile, Acta Mater. **51**, 5981 (2003).
[5]R. Doshi, V. Richards, and J. Carter, J. Electrochem. Soc. **146**, 1273 (1999).
[6]S. Tao and J. T. S. Irvine, Nat. Mater. **2**, 320 (2003).
[7]J. C. Ruiz-Morales, J. Canales-Vázquez, C. Savaniu, D. Marrero-López, W. Zhou, and J. T. S. Irvine, Nature **439**, 568 (2006).

[8]T. Hibino, A. Hashimoto, T. Inoue, J. Tokuno, S. Yoshida, and S. Mitsuru, Science **288**, 2031 (2000).
[9]I. Fullarton, J. Jacobs, H. Van Benthem *et al.*, Ionics (Kiel) **1**, 51 (1995).
[10]Y.-L. Lee, J. Kleis, J. Rossmeisl, and D. Morgan, Phys. Rev. B **80**, 224101 (2009).
[11]S. J. Skinner, Int. J. Inorg. Mater. **3**, 113 (2001).
[12]F. W. Poulsen, Solid State Ionics **129**, 145 (2000).
[13]S. P. Jiang, J. Mater. Sci. **43**, 6799 (2008).
[14]A. Thursfield and I. S. Metcalfe, J. Membr. Sci. **288**, 175 (2007).
[15]T. Arima and Y. Tokura, J. Phys. Soc. Jpn. **64**, 2488 (1995).
[16]T. Arima, Y. Tokura, and J. Torrance, Phys. Rev. B **48**, 15 (1993).
[17]M. Cherry, M. S. Islam, and C. R. A. Catlow, J. Solid State Chem. **118**, 125 (1995).
[18]Y. A. Mastrikov, E. Heifets, E. A. Kotomin, and J. Maier, Surf. Sci. **603**, 326 (2009).
[19]S. M. Woodley, J. D. Gale, P. D. Battle, and C. R. A. Catlow, J. Chem. Phys. **119**, 9737 (2003).
[20]M. J. Koponen, M. Suvanto, K. Kallinen, T.-J. J. Kinnunen, M. Härkönen, and T. A. Pakkanen, Solid State Sci. **8**, 450 (2006).
[21]L. E. Smart and A. E. Moore, *Solid State Chemistry: An Introduction*, 4th ed. (CRC Press, 2012).
[22]M. Dine El Hannani, D. Rached, M. Rabah, R. Khenata, N. Benayad, M. Hichour, and A. Bouhemadou, Mater. Sci. Semicond. Process. **11**, 81 (2008).
[23]A. Orera and P. R. Slater, Chem. Mater. **22**, 675 (2010).
[24]J. B. Goodenough, Annu. Rev. Mater. Res. **33**, 91 (2003).
[25]M. A. Peña and J. L. Fierro, Chem. Rev. **101**, 1981 (2001).
[26]Y. Wang, X. Zhao, S. Lü, X. Meng, Y. Zhang, B. Yu, X. Li, Y. Sui, J. Yang, C. Fu, and Y. Ji, Ceram. Int. **40**, 11343 (2014).
[27]J. A. Kilner and M. Burriel, Annu. Rev. Mater. Res. **44**, 365 (2014).
[28]J. Van Herle, A. J. J. Mcevoy, and K. R. Thampi, Electrochim. Acta **41**, 1447 (1996).
[29]R. A. De Souza, J. A. Kilner, and J. F. Walker, Mater. Lett. **43**, 43 (2000).
[30]T. Ishihara, J. Electrochem. Soc. **145**, 3177 (1998).
[31]M. Arshad Farhan and M. Javed Akhtar, J. Phys.: Condens. Matter **22**, 075402 (2010).
[32]K. H. Jung, S. Choi, H.-H. Park, and W.-S. Seo, Curr. Appl. Phys. **11**, S260 (2011).
[33]M. C. Pearce and V. Thangadurai, Ionics **14**, 483 (2008).
[34]C. Xia, W. Rauch, F. Chen, and M. Liu, Solid State Ionics **149**, 11 (2002).
[35]M. Liu, M. E. Lynch, K. Blinn, F. M. Alamgir, and Y. Choi, Mater. Today **14**, 534 (2011).
[36]J. Fleig, Annu. Rev. Mater. Res. **33**, 361 (2003).
[37]H. Tu and Y. Takeda, Solid State Ionics **100**, 283 (1997).
[38]S. Pawar, K. Shinde, A. Bhosale, and S. Pawar, J. Mater. **2013**, 987328 (2013).
[39]N. K. Gaur and R. Thakur, Metall. Mater. Trans. A **44**, 5876 (2013).
[40]N. B. Ivanova, N. V. Kazak, C. R. Michel, a. D. Balaev, and S. G. Ovchinnikov, Phys. Solid State **49**, 2126 (2007).
[41]K. Knížek, Z. Jirák, J. Hejtmánek, M. Veverka, M. Maryško, G. Maris, and T. T. M. Palstra, Eur. Phys. J. B **47**, 213 (2005).
[42]P.-H. Xiang, S. Asanuma, H. Yamada, H. Sato, I. H. Inoue, H. Akoh, A. Sawa, M. Kawasaki, and Y. Iwasa, Adv. Mater **25**, 2158 (2013).
[43]Z. Jirák, J. Hejtmánek, K. Knížek, P. Novák, E. Šantavá, and H. Fujishiro, J. Appl. Phys. **115**, 17E118 (2014).
[44]J. H. Kuo and H. U. Anderson, J. Solid State Chem. **83**, 52 (1989).
[45]R. A. De Souza, M. S. Islam, and E. Ivers-Tiffée, J. Mater. Chem. **9**, 1621 (1999).
[46]J. Nowotny and M. Rekas, J. Am. Ceram. Soc. **81**, 67 (1998).
[47]A. A. Leontiou, A. K. Ladavos, T. V Bakas, T. C. Vaimakis, and P. J. Pomonis, Appl. Catal., A **241**, 143 (2003).
[48]J. Mizusaki, N. Mori, H. Takai, and Y. Yonemura, Solid State Ionics **129**, 163 (2000).
[49]T. I. Arbuzova, V. I. Voronin, B. a. Gizhevskiĭ, S. V. Naumov, and V. L. Arbuzov, Phys. Solid State **52**, 1217 (2010).
[50]P. J. Shen, X. Liu, H. H. Wang, and W. Z. Ding, Solid State Sci. **13**, 276 (2011).
[51]M. Pavone, A. B. Muñoz-Garcia, A. M. Ritzmann, and E. A. Carter, J. Phys. Chem. C **118**, 13346 (2014).
[52]E. A. Kotomin, Y. A. Mastrikov, M. M. Kuklja, R. Merkle, A. Roytburd, and J. Maier, Solid State Ionics **188**, 1 (2011).
[53]G. Kresse and J. Hafner, Phys. Rev. B **47**, 558 (1993).
[54]G. Kresse and J. Hafner, Phys. Rev. B **49**, 14251 (1994).
[55]G. Kresse and J. Furthmüller, Comput. Mater. Sci. **6**, 15 (1996).
[56]G. Kresse and J. Furthmüller, Phys. Rev. B: Condens. Matter Mater. Phys. **54**, 11169 (1996).
[57]P. E. Blöchl, Phys. Rev. B **50**, 17953 (1994).
[58]J. Perdew, K. Burke, and M. Ernzerhof, Phys. Rev. Lett. **77**, 3865 (1996).
[59]J. Perdew, K. Burke, and M. Ernzerhof, Phys. Rev. Lett. **78**, 1396 (1997).
[60]P. E. Blöchl, O. Jepsen, and O. K. Andersen, Phys. Rev. B **49**, 16223 (1994).
[61]H. J. Monkhorst and J. D. Pack, Phys. Rev. B **13**, 5188 (1976).
[62]R. F. W. Bader, *Atoms in Molecules: A Quantum Theory* (Oxford University Press, Oxford, 1990).
[63]G. Henkelman, A. Arnaldsson, and H. Jónsson, Comput. Mater. Sci. **36**, 354 (2006).
[64]T. Geng, Z. Han, and S. Zhuang, Phys. B: Condens. Matter **405**, 3714 (2010).
[65]P. Ravindran, A. Kjekshus, H. Fjellvåg, A. Delin, and O. Eriksson, Phys. Rev. B **65**, 064445 (2002).
[66]P. Ravindran, R. Vidya, H. Fjellvåg, and A. Kjekshus, J. Cryst. Growth **268**, 554 (2004).
[67]S. Dudarev, G. Botton, and S. Savrasov, Phys. Rev. B **57**, 1505 (1998).
[68]A. M. Ritzmann, M. Pavone, A. B. Muñoz-García, J. A. Keith, and E. A. Carter, J. Mater. Chem. A **2**, 8060 (2014).
[69]S. Zhang, N. Han, and X. Tan, RSC Adv. **5**, 760 (2015).
[70]Z. Alahmed and H. Fu, Phys. Rev. B **76**, 224101 (2007).
[71]E. Heifets, S. Piskunov, E. A. Kotomin, Y. F. Zhukovskii, and D. E. Ellis, Phys. Rev. B **75**, 115417 (2007).
[72]A. M. Ritzmann and A. B. Muñoz-García, Chem. Mater. **25**, 3011 (2013).
[73]P. G. Sundell, M. E. Björketun, and G. Wahnström, Phys. Rev. B **73**, 104112 (2006).
[74]H. Raebiger, S. Lany, and A. Zunger, Phys. Rev. B **76**, 045209 (2007).
[75]T. Tanaka, K. Matsunaga, Y. Ikuhara, and T. Yamamoto, Phys. Rev. B **68**, 205213 (2003).
[76]C. G. Van De Walle and J. Neugebauer, J. Appl. Phys. **95**, 3851 (2004).
[77]D. O. Scanlon, J. Buckeridge, C. R. A. Catlow, and G. W. Watson, J. Mater. Chem. C **2**, 3429 (2014).
[78]C. Freysoldt, B. Grabowski, T. Hickel, J. Neugebauer, G. Kresse, A. Janotti, and C. G. Van De Walle, Rev. Mod. Phys. **86**, 253 (2014).
[79]J. Buckeridge, D. O. Scanlon, A. Walsh, and C. R. A. Catlow, Comput. Phys. Commun. **185**, 330 (2014).
[80]S. W. Baek, J. H. Kim, and J. Bae, Solid State Ionics **179**, 1570 (2008).
[81]M. W. Chase, *NIST-JANAF Thermochemical Tables* (American Chemical Society, 1998).
[82]A. Wold and R. Ward, J. Am. Chem. Soc. **76**, 1029 (1954).
[83]R. Scurtu, S. Somacescu, J. M. Calderon-Moreno, D. Culita, I. Bulimestru, N. Popa, A. Gulea, and P. Osiceanu, J. Solid State Chem. **210**, 53 (2014).
[84]T. Saitoh, T. Mizokawa, A. Fujimori, and M. Abbate, Phys. Rev. B **55**, 4257 (1997).
[85]F. A. Kröger and H. J. Vink, Solid State Phys. **3**, 307 (1956).
[86]A. Alkauskas, P. Broqvist, and A. Pasquarello, Phys. Status Solidi Basic Res. **248**, 775 (2011).
[87]J. Perez-Cacho, J. Blasco, J. Garcia, and R. Sanchez, J. Solid State Chem. **150**, 145 (2000).
[88]J. H. Kim, M. Cassidy, J. T. S. Irvine, and J. Bae, J. Electrochem. Soc. **156**, B682 (2009).
[89]H. Shimada, T. Yamaguchi, T. Suzuki, H. Sumi, K. Hamamoto, and Y. Fujishiro, J. Power Sources **302**, 308 (2016).
[90]C. Persson, Y. J. Zhao, S. Lany, and A. Zunger, Phys. Rev. B: Condens. Matter Mater. Phys. **72**, 1 (2005).